Journal of Inorganic and Organometallic Polymers and Materials (2021) 31:2293–2305
https://doi.org/10.1007/s10904-021-01916-3

Synergistic Catalytic Effect of Thermite Nanoparticles on HMX Thermal Decomposition

Sherif Elbasuney[1,2] · M. Yehia[2] · Abdelaziz Hamed[2] · Mohamed Mokhtar[2] · Mohamed Gobara[2] · Ahmed Saleh[3] · Eslam Elsaka[2] · Gharieb S. El-Sayyad[2,4]

Received: 22 August 2020 / Accepted: 23 January 2021 / Published online: 18 February 2021

Abstract

Even though HMX is one of the most vigorous energetic materials for solid propellants, explosives, and pyrotechnics; it has high thermal stability and low sensitivity to common catalysts. Metal oxides with hydrous surface can release active ȮH radicals at low temperature. These active radicals could attack HMX heterocyclic ring and alter HMX decomposition mechanism form C-H bond cleave to hydrogen atom abstraction. This study reports on the facile synthesis of Fe_2O_3 nanoparticles (NPs) of 8 nm average particle size. Aluminum NPs of 80 nm was employed in combination with Fe_2O_3 NPS; this nanothermite binary mixture can induce not only catalytic effect but also vigorously-exothermic thermite reaction with high heat output. Colloidal thermite mixture Fe_2O_3/Al was effectively-integrated into HMX crystals via co-precipitation technique. Uniform distribution of nanothermite particles into HMX was confirmed via elemental mapping using EDAX. Nanothermite mixture as high energy density material offered an increase in HMX total heat release by 82% using DSC. Furthermore, nanothermite particles offered superior catalytic effect with decrease in HMX activation energy by 25% using Kissinger method. Kinetic decomposition parameters using KAS model were found to be in good agreement with Kissinger's model. Colloidal nanothermite particles can act as high energy density material, and as a catalyst with decrease in required activation energy.

Keywords Energetic materials · Thermal behavior · Catalyst · Nanoparticles · Hydrothermal synthesis

1 Introduction

Energetic nanocomposite can offer novel performance characteristics in terms of combustion enthalpy as well as thermal decomposition kinetics [1, 2]. HMX ($C_4H_8N_8O_8$) is one of the most common energetic materials for solid propellants, explosives, and pyrotechnics [3]. HMX can offer high detonation heat, large amount of gaseous products with low molecular weight [4, 5]. However HMX is insensitive to common catalysts [6]. Combustion performance of HMX is affected by its thermal decomposition. Nano-catalysts (i.e. TiO_2) with high specific surface areas and surface activations are widely mixed-with HMX to regulate its thermal properties [4]. However, Fe_2O_3 has been widely-employed as catalyst in solid propellants [7]. Fe_2O_3 particles have hydrous surface (plenty of hydroxyl groups are bonded to the particle surface) [8]. The strength of surface-bounded –OH groups is a key parameter for metal oxide catalytic activity evaluation. Electro-negativity of metal cation x_i expresses the capability to withdraw electron pair (Eq. 1) [9].

$$\mathbf{X_i = X_o \times (1 - 2n)}$$

where x_o, and n are electronegativity of metal atom, the metal charge in the oxide state. Metal oxide with high X_i have acid properties, oxides with low X_i have base properties [9]. The correlation between reaction rate and electronegativity for different oxides is demonstrated in Fig. 1 [9].

✉ Sherif Elbasuney
s.elbasuney@mtc.edu.eg; sherif_basuney2000@yahoo.com

✉ Gharieb S. El-Sayyad
Gharieb.Elsayyad@eaea.org.eg;
Gharieb.Elsayyad2017@gmail.com

1 Head of Nanotechnology Research Center, School of Chemical Engineering, Military Technical College (MTC), Egyptian Armed Forces, Cairo, Egypt

2 School of Chemical Engineering, Military Technical College (MTC), Egyptian Armed Forces, Cairo, Egypt

3 Science and Technology Center of Excellence, Cairo, Egypt

4 Drug Radiation Research Department, National Center for Radiation Research and Technology (NCRRT), Egyptian Atomic Energy Authority (EAEA), Cairo, Egypt

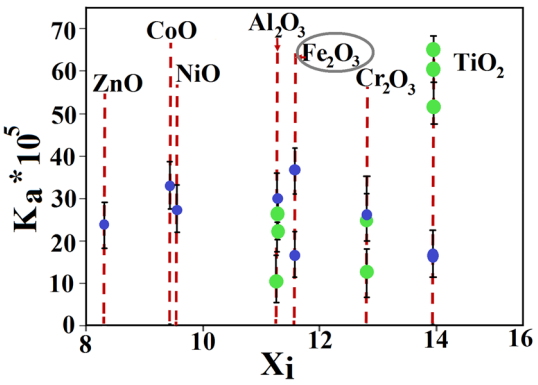

Fig. 1 Catalytic efficiency of different oxides according to cation electro-negativitiy; where nanoparticles in green color & micronparticles in blue color [9]

The bound energy of surface –OH groups is a vital factor controlling the catalytic activity of oxide particles. Fe_2O_3 NPs can offer low bound energy of –OH surface; therefore they can offer superior efficiency compared with other oxides [10, 11]. Fe_2O_3 nanocatalyst can secure superior catalytic performance. Fe_2O_3 NPs could offer high release rate of active ȮH radicals; these radicals could attack HMX heterocyclic ring. While HMX decomposition is C–H bond cleavage of heterocyclic ring; Fe_2O_3 NP_S can alter HMX decomposition via hydrogen atom abstraction of heterocyclic ring [4]. Therefore, decomposition process could occur at high rate and at low temperature. This catalytic mechanism could offer low activation energy [12]. Additionally, Fe_2O_3 can induce vigorously-exothermic thermite reaction with aluminum NPs. Such thermite mixture can boost the decomposition enthalpy, and in the meantime could further boost HMX decomposition [13, 14].

Core-shell nanocomposites composed of Fe_3O_4 NPs and conjugated polymer, were successfully-synthesized from a simple and inexpensive in situ chemical oxidative polymerization [15, 16]. The synthesized Fe_3O_4-based nanocomposites possesses a relatively-high magnetic features [17, 18], and can be used in photo-electrochemical water oxidation, that based on co-doped α-Fe_2O_3 nanostructure photo-anode [19]. Some development nanostructured magnetic metal oxides and its biopolymer hybrids can be used also for the biomedical application, and the synthetic methods influencing the parameters which essential for the biomedical purposes, including antimicrobial, antioxidant, and anticancer applications [20–23], and environmental usage as photocatalysts for high efficiency photocatalytic degradation of toxic organic pollutants from wastewater [24–26].

There are different techniques and highly-effective nanomaterials used for decomposition of hazardous chemicals such as textile waste, dyes/inorganic salts separation of cerium oxide-loaded loose nano-filtration polyethersulfone membranes [27], photocatalytic activity of graphene-organic frameworks (GOFs), and metal-OF [28, 29], application of Ni-, Fe-, Mn-, and Cu-doped ZrO_2 NPs [30–33], membrane-based separation of potential emerging pollutants [34], utilization of gadolinium substituted $BiFeO_3$ NPs, and $BiVO_4$ nanostructures [35, 36], the potential of barium titanate nanostructures for photo-degradation of chemical pollutants [37], usage of ZnO nanosheets-decorated Bi_2WO_6 nanolayers [38], and novel Co, and Ni nanostructures for the photo-degradation of organic dyes [39].

This study reports on the facile fabrication of colloidal Fe_2O_3 NPs of 8 nm average particle size using hydrothermal synthesis. Aluminum NPs in the shape of nano-plates of 80 nm particle size were employed. Colloidal mixture (Fe_2O_3/Al) was effectively-integrated into HMX crystalline structure via co-precipitation technique. Uniform dispersion of Fe_2O_3 and aluminum NPs into HMX was verified via elemental mapping using SEM.

Nanothermite particles can act as novel catalyst and high energy density material; Fe_2O_3/Al/HMX nanocomposite demonstrated superior combustion characteristics with an increase in total heat release by 82%. Additionally, Fe_2O_3 NPs can offer as novel catalyst for HMX thermolysis. The catalytic activity of Fe_2O_3/Al on HMX thermolysis was evaluated via investigation of kinetic parameters using Kissinger method. Nanothermite particles offered decrease in HMX activation energy by 25%. Nanothermite particles could alter the decomposition mechanism of HMX to hydrogen atom abstraction instead of C–H cleavage [3, 40]. It can be concluded that thermite particles not only act as high energy density material but also it could act as a sensitizer with decrease in required activation energy.

2 Experimental Methods

2.1 Development of HMX Nanocomposite

Fe_2O_3 NPs were synthesized using hydrothermal processing. Further details about the hydrothermal synthesis can be found in the following references [8, 41, 42]. Fe_2O_3 colloidal particles demonstrated stable colloid; this was ascribed to electrostatic stabilization. Fe_2O_3 NPs were harvested from their synthesis medium, and re-dispersed in organic solvent. The total loading level of thermite nanoparticles was 6 wt%. Stoichiometric mixture of Fe_2O_3/Al was (3:1). Fe_2O_3 NPs was re-dispersed into acetone; subsequently HMX was dissolved in acetone colloid. The hybrid nanocomposite material was developed by co-precipitation technique as demonstrated in Fig. 2, and the source (company name, grade, and country) of chemicals, and materials was displayed in Table S1 (Supplementary material).

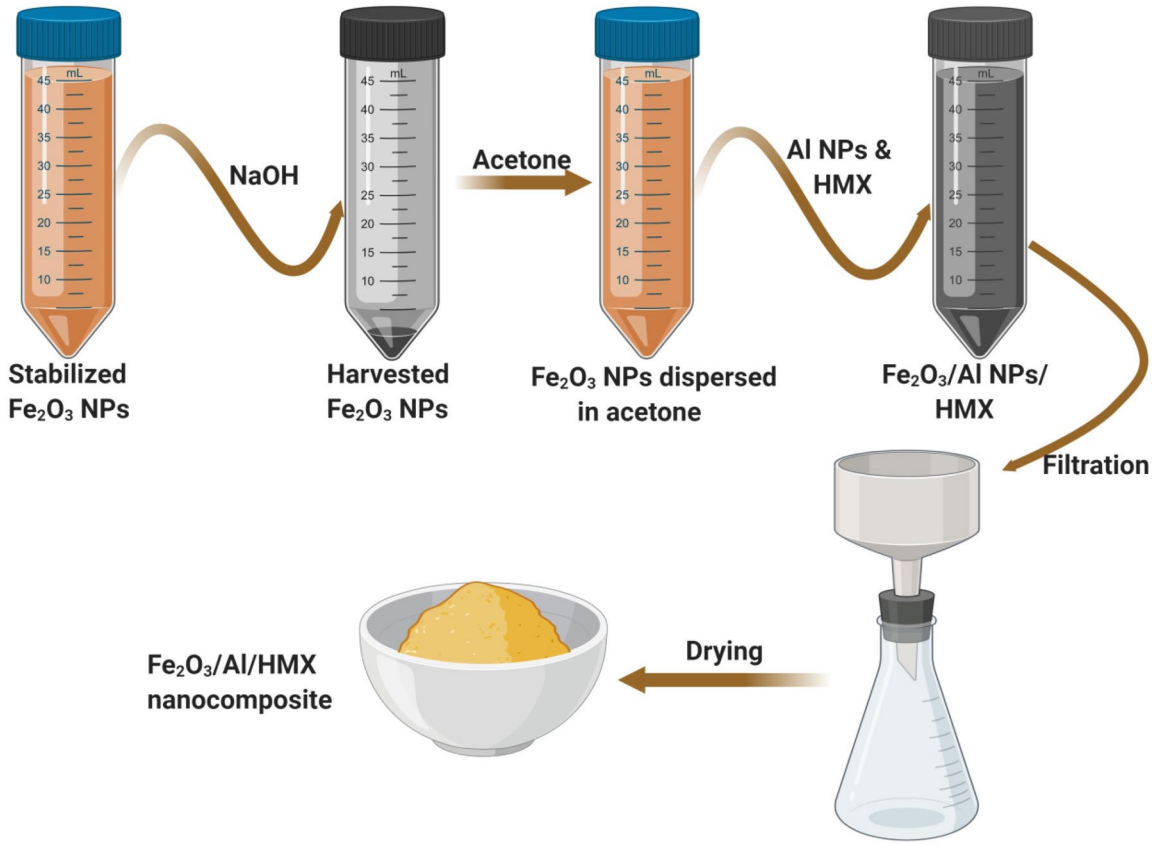

Fig. 2 Development of Fe_2O_3/Al/HMX nanocomposite via co-precipitation technique

2.2 Characterization of Nanoparticles and Nanocomposite

Shape and sizes of the synthesized colloidal Fe_2O_3 and Al NPs was visualized using HRTTEM (JEM-2100F by Joel Corporation). The crystalline structure and crystal size were investigated with XRD, XTRA Powder diffractometer by Thermo Scientific. The strength of the diffracted X- rays was recognized as the diffracted angle 2θ. Morphology and surface properties of the developed HMX-hybrid nanocomposites was investigated with SEM, ZEISS SEM EVO 10 MA. Also, EDX spectrum examination (BRUKER, Nano GmbH, D-12489, 410-M, Germany) was used to estimate the elemental composition, purity and the relationship of each metal in HMX-hybrid nanocomposites. FT-IR analysis was carried out by a JASCO FT-IR 3600 (400-4000 cm^{-1} wavenumber) to determine OH surface function group in Fe_2O_3 NPs. Finally, the SEM/EDX mapping method was directed for giving further information regarding the simplicity, relationships, and the position of the metals which may be founded in the synthesized HMX-hybrid nanocomposites.

2.3 Thermal Behaviour of HMX Nanocomposite

Thermite nanoparticles can offer vigorous exothermic reaction with an increase in the total heat output. Thermal behavior of HMX nanocomposite was investigated using DSC Q20 by TA. Nanocomposite sample was heated from 50 to 500 °C, at 5 °C min^{-1}. The impact of thermite NPs on HMX weight loss was investigated using TGA 55 by TA. The tested sample was heated from 50 to 500 °C, at 5 °C min^{-1}.

2.4 Kinetic Study of Fe_2O_3/Al/HMX Nanocomposite

Many available analytical methods can be employed to determine the kinetic parameters of solid-phase reactions. Isoconversional (model-free) and model fitting methods are considered the two main methods to determine the kinetic parameters that can be evaluated either isothermally or non-isothermally [43].

The impact of nanothermite particles on HMX kinetic parameters (i.e. activation energy) was evaluated using TGA. TGA experiments were carried out with four heating rate 2, 3, 4, 5 and 10 °C·min^{-1}. The third kinetics

parameters including pre-exponential factor (A), kinetic model (f(α)) and activation energy (E_a) were evaluated for the kinetic analysis.

2.4.1 Activation Energy Calculation

The activation energy (E_a) of sample decomposition reaction can be calculated from Kissinger's method (Eq. 2)

$$-\frac{Ea}{R} = \frac{d\ln\left(\beta/T_p^2\right)}{d\left(1/T_p\right)} \quad (2)$$

where: β and Tp are the heating rate, DTG peak temperature at that rate, respectively. The activation energy (E_a) can be calculated from the slop of the straight line of ln (β/Tp^2) versus 1/Tp [44, 45]. More accurate equation was presented according to Starink for activation energy determination. This model is commonly-called the Kissinger–Akahira–Sunose (KAS) Equation [46].

$$\ln\left(\frac{\beta_i}{T_{\alpha,i}^{1.92}}\right) = \text{Const} - 1.0008\frac{E\alpha}{RT\alpha}$$

3 Results and Discussions

3.1 Characterization of Thermite Nanoparticles

XRD system was conducted to study the crystal composition and state of the incorporated Fe_2O_3 and Al NPs (Fig. 3).

Ferric oxide XRD model agree to the specific α-Fe_2O_3 original (JCPDS No. 33-0664). The unique peaks looked at the next 2θ arranges ≈ 24.12°, 33.18°, 35.60°,40.72°, 49.50°, 54.15°, 57.43°, and 64.11° and corresponding to (012, 104, 110, 113, 024, 116, 018, and 300) planes, respectively and therefore showing its cubic spinel composition [47]. This matches with the unique composition of the standard α-Fe_2O_3 crystal and corresponding to JCPDS card number 33-0664 [48–52]. Williamson-Hall (W–H) method was applied to define the common crystallite size of the processed metal-oxides NPs [53–57], according to Eq. 4. The most important diffraction peak near 35.60° implies that (110) facets remain the dominant α-Fe_2O_3 crystal construction with 12.20 nm crystal size according to Williamson–Hall (W–H).

$$\beta\cos\theta = \frac{k\lambda}{D_{W-H}} + 4\varepsilon\sin\theta$$

where DW-H is the average crystallite size, λ is the X-ray wavelength, k is a shape constant, β is the full-width at half maximum, ε is the sample strain and θ is the Bragg's angle of diffraction.

On the other hand, The XRD data of the Al NPs in Fig. 3 shows the structure of the diffraction properties owns 2θ at 38.45°, 45.15°, 66.19° and 78.41° which represent the Bragg's reflections at (111), (200), (220), and (311), respectively [58]. The presented peaks were similar with the Joint Committee on Powder Diffraction Standards (JCPDS) of Al NPs (JCPDS Card No: 00-004-0787) [58–60]. According to Williamson–Hall (W–H) Eq. (4), the crystal size for Al NPs was calculated to be 80 nm. XRD diffractogram demonstrated highly-crystalline structure.

HRTEM images of the synthesized Fe_2O_3 NPs confirmed mono-dispersed NPs with an average particle size of 8 nm (Fig. 4a). This result was a great match to the reported XRD pattern in Fig. 3, where α-Fe_2O_3 was the principal crystal form of the processed sample. On the other hand, the HRTEM images of the prepared Al NPs (Fig. 4b) demonstrated the nano-flakes with average particle size of 80 nm.

Appearance, surface morphology and elemental analysis of the prepared Fe_2O_3 NPs are represented in SEM imaging and EDX spectrum as in Fig. 5. EDX spectroscopy was employed to analyze the elemental structure and to validate the prepared samples chemically [54, 55, 61, 62].

It can be recognized from Fig. 5a that Fe_2O_3 NPs presented as bright particles, and were uniformly-dispersed. Figure 5b represented the elemental composition of the synthesized Fe_2O_3 NPs, where both Fe and O atoms were belonged to the produced Fe_2O_3 NPs. The elemental mappings of the prepared Fe_2O_3 NPs are displayed in Fig. 6.

All images were identified as O (green color), and Fe (red color). From this imaging, it is obvious that Fe_2O_3 NPs was similar in terms of the appearance of Fe and O atoms where both of them, are homogenously-distributed.

Similarly, Fig. 7a shows the SEM analysis and the corresponding EDX pattern (Fig. 7b) of Al NPs which also

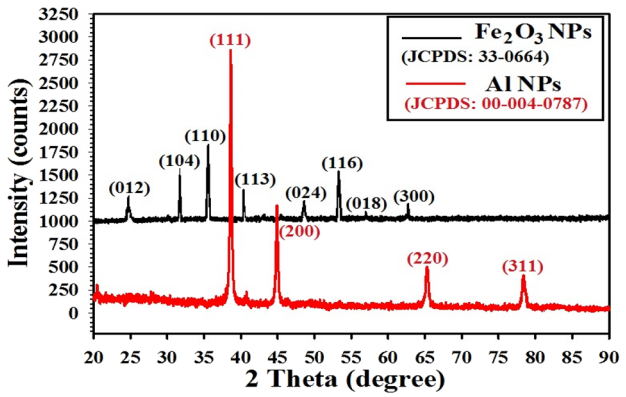

Fig. 3 Crystallinity and crystal phase determination by XRD analysis for the synthesized Fe_2O_3 NPs and Al NPs

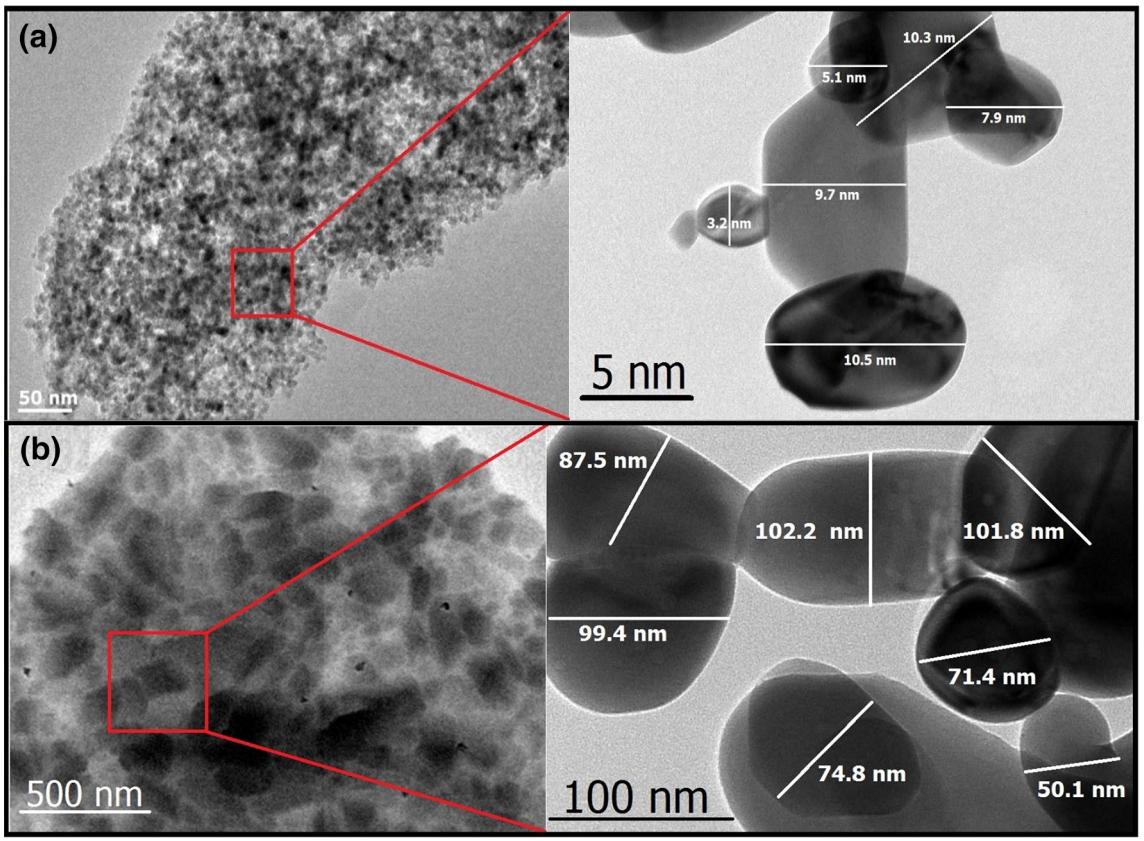

Fig. 4 Shape and particle size determination by HRTEM imaging for the synthesized Fe_2O_3 NPs (**a**), and Al NPs (**b**)

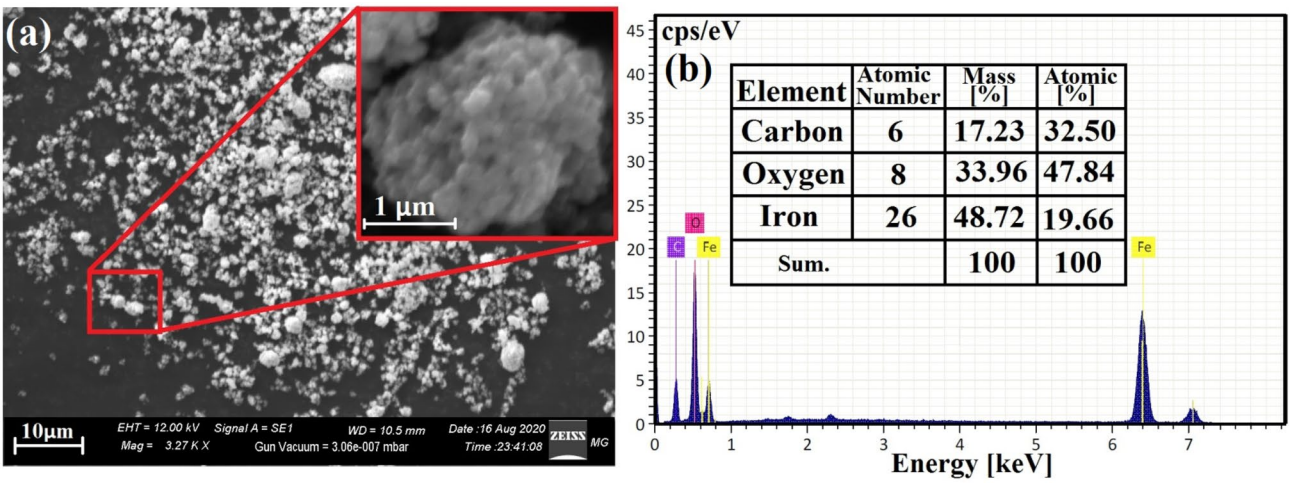

Fig. 5 Surface morphology determination, and elemental analysis by SEM imaging (**a**), and EDX (**b**) for the synthesized Fe_2O_3 NPs

appeared as bright and irregular flacks and were displayed as Al in EDX analysis with traces of O atoms could be correlated to protective oxide layer of Al_2O_3.

Additionally, the elemental mappings of the prepared Al NPs are displayed in Fig. 8. All images were identified as Al (pink color), and O (green color). From this imaging, it is obvious that Al NPs was similar in terms of the appearance of Al atom, and homogenously-distributed. The traces of oxygen (green color) were attributed to the passive oxide layer on the surface.

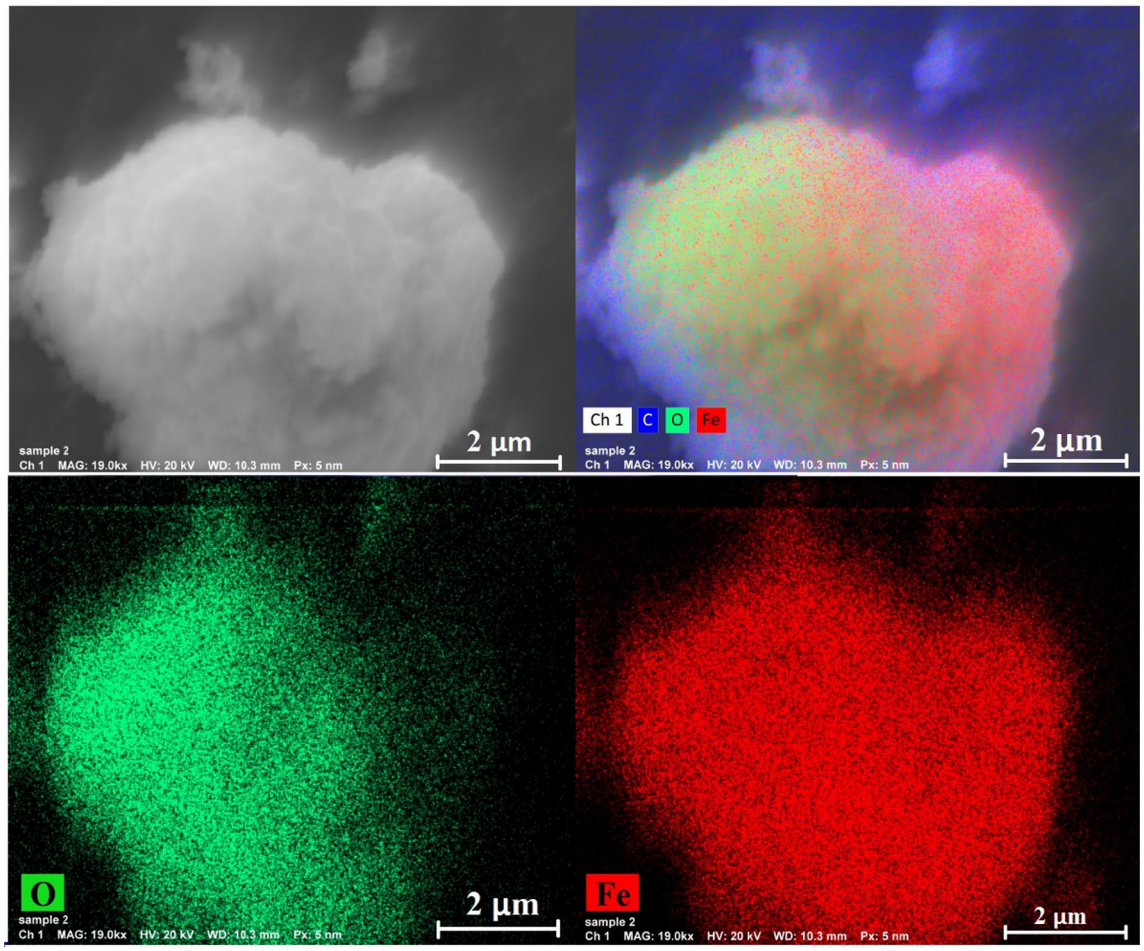

Fig. 6 Elemental mapping of Fe_2O_3 NPs and distributed as O, and Fe atoms

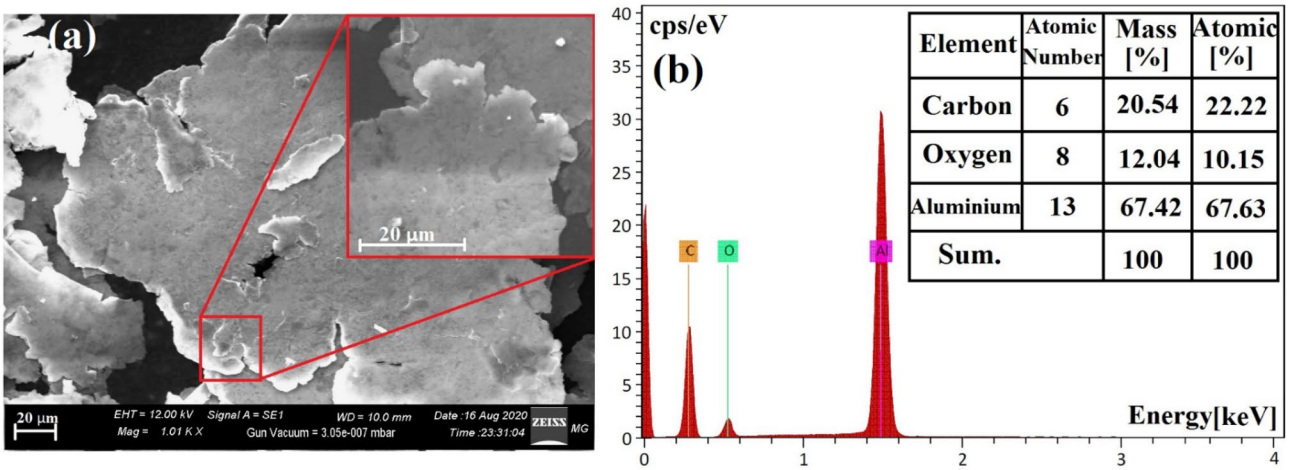

Element	Atomic Number	Mass [%]	Atomic [%]
Carbon	6	20.54	22.22
Oxygen	8	12.04	10.15
Aluminium	13	67.42	67.63
Sum.		100	100

Fig. 7 Surface morphology determination, and elemental analysis by SEM imaging (**a**), and EDX (**b**) for the synthesized Al NPs

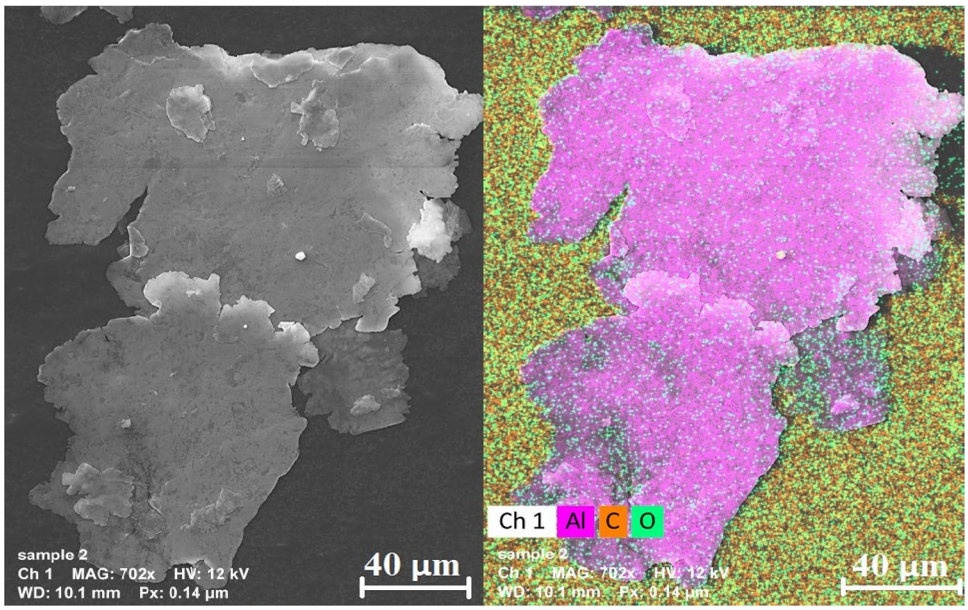

Fig. 8 Elemental mapping of Al NPs and distributed as C, O, and Al atoms

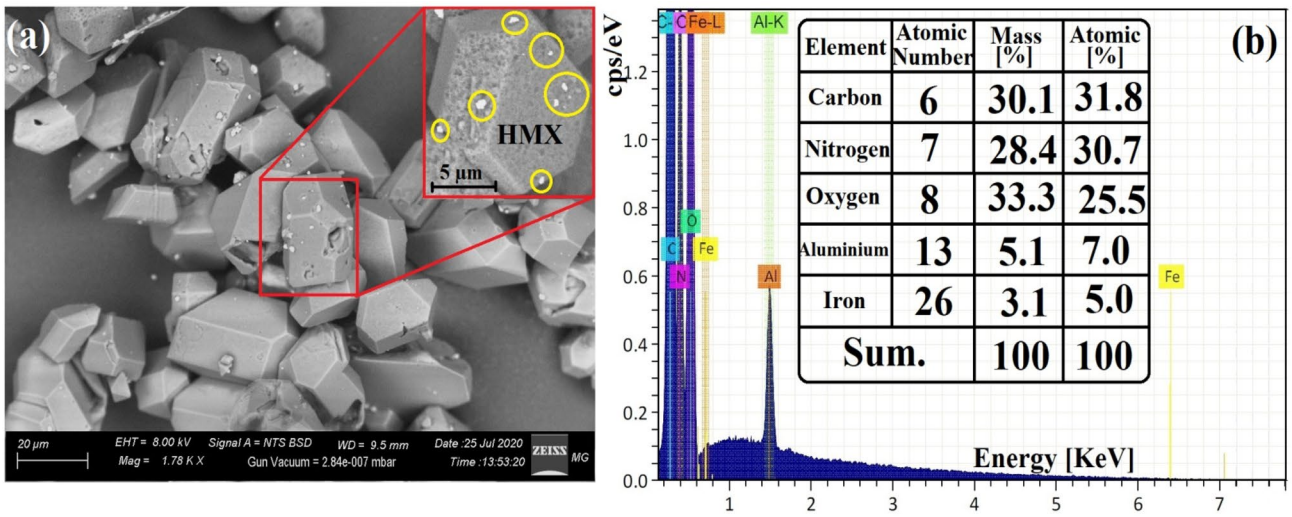

Fig. 9 SEM micrographs of the synthesized HMX-thermite nanocomposite (**a**), and EDX elemental analysis of HMX-thermite powder (**b**)

3.2 Characterization of HMX Nanocomposites

The surface characteristics and morphology of HMX nanocomposite were investigated by applying the SEM technique. SEM micrographs of developed HMX nanocomposite demonstrated cubic shapes with average particle size of 50 µm (Fig. 9a). It can be noticed that thermite NPs (Fe_2O_3 and Al) were evenly-distributed into HMX. Thermite particles were characterized as brilliant NPs linked to HMX units.

EDX analysis was employed to establish the elemental composition of the synthesized HMX- nanocomposites. The elemental composition of the HMX-thermite nanocomposites is represented in Fig. 9b.

The synthesized HMX-thermite nanocomposites exhibited notable absorption peaks of the iron element at 6.4 keV and 1.45 keV, Oxygen element at 0.45 keV for Fe_2O_3 NPs. Additionally, aluminum element present at 1.45 keV for Al NPs, and finally, carbon (0.25 keV), oxygen (0.45 keV), and nitrogen (0.38 keV) elements were corresponding to HMX compound. The lack of further elemental peaks confirms the purity of the synthesized HMX-thermite nanocomposite. HMX nanocomposite with uniform particle size of 50 µm was developed via co-precipitation technique.

The elemental mapping of the integrated HMX-thermite nanocomposite verified the formation of the nanocomposite in terms of its components (N, C, O, Fe, and Al atoms) (Fig. 10). N atom (yellow color), O atom (pink color), and

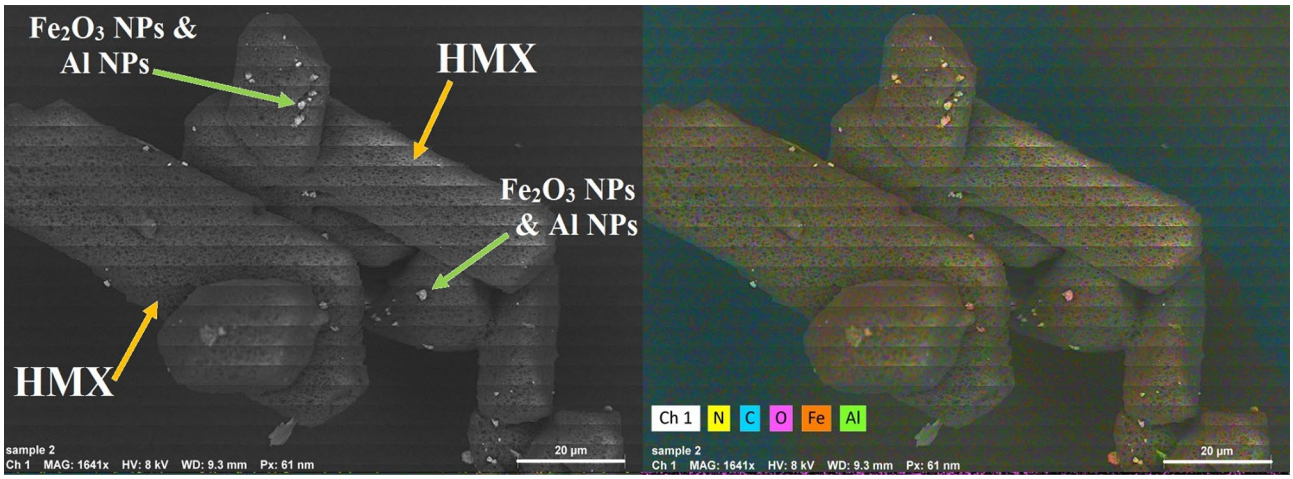

Fig. 10 Elemental mapping of Fe_2O_3 NPs and Al NPs integrated into HMX and distributed as N, C, O, Fe and Al atoms

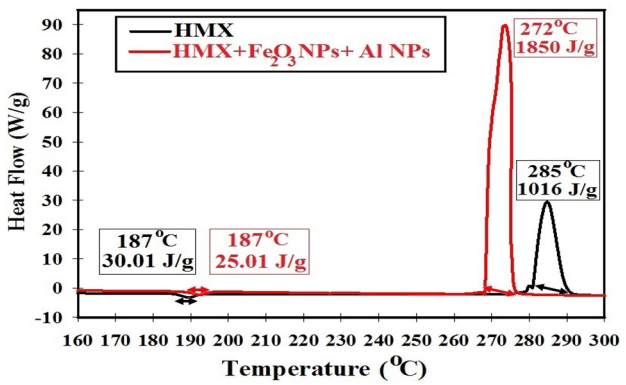

Fig. 11 Impact of thermite nanoparticles on HMX thermal behavior using DSC analysis

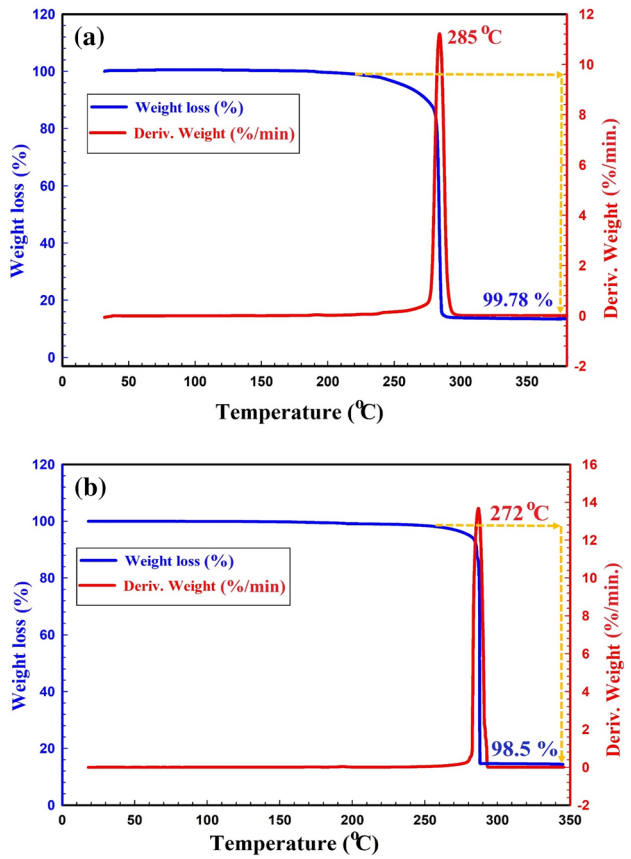

Fig. 12 TGA thermogram of HMX (**a**), Fe_2O_3/Al/HMX nanocomposite (**b**)

C atom (faint blue) were corresponding to HMX molecules (HMX molecular formula; $C_4H_8N_8O_8$), also Fe bright NPs (orange color) and O atom (pink color) were related to the synthesized Fe_2O_3 NPs, finally, Al bright NPs (green color) was assigned for Al NPs.

Interestingly, images of elemental mapping confirmed the effective integration of colloidal thermite particles (Fe_2O_3 & Al NPs) into HMX. This approach could secure highly-hydrous surface as well as high interfacial surface area. Elemental mapping using SEM/EDX coupled technique confirmed uniform dispersion of Fe_2O_3 and Al NPs into HMX.

3.3 Thermal Behaviour of HMX Nanocomposite

Integration of thermite NPs as high energy density materials into HMX demonstrated dramatic change in HMX thermal behavior. HMX nanocomposite offered an increase in total heat release by 82% compared with virgin HMX. Additionally, the main decomposition temperature was decreased by 13 °C as demonstrated via DSC thermogram (Fig. 11).

It is widely-accepted that thermite particles can secure vigorous exothermic reaction with an increase in total heat

release [2]. The catalytic activity of thermite NPs was further evaluated with TGA; TGA thermograms confirmed DSC outcomes. Temperature at total weight loss was decreased by 13 °C. Figure 12a, and b demonstrate the thermal behavior of HMX and HMX nanocomposite, respectively.

Thermite NPs demonstrated decrease in HMX main decomposition temperature by 13 °C; this could be ascribed to the catalytic effect of thermite particles. Additionally, Fe_2O_3 NPs with their hydrous surface could alter mechanism of HMX from C-H bond cleavage to H atom abstraction [4]. The mechanism can be summarized as follow:

(1) Fe_2O_3 NPs can offer high ability to release active ȮH radicals; the evolved radicals would be capable to abstract hydrogen atom from HMX heterocyclic ring [63].
(2) Energy of N–NO_2 bond would be decreased; nitro group could be released more easily form HMX molecule [64].
(3) Evolved NO_2 group could attack another HMX molecule and abstract an H-atom (Fig. 13).

Adsorption of NO_2 and decomposition gaseous products on the surface of Fe_2O_3 NPs could induce highly-exothermic reaction within the condensed phase with an increase in the total heat release [9]. Furthermore, thermite NPs could offer enhanced heat output and the thermal conductivity with lower decomposition temperature.

In order to evaluate the functionality of ferric oxide particles with OH functional groups; FTIR analysis was conducted. FT-IR spectrum was a significant study that provides important data about the chemical functional groups represented in Fe_2O_3 NPs [65]. FTIR spectrum of developed Fe_2O_3 NPs confirmed the hydrous surface. The enhanced levels of IR absorption at 3520 cm^{-1} can be correlated to the O–H surface group stretch as shown in Fig. 14. The Fe–O was appearing at the 603 cm^{-1}. This result was matched with the results described in previous publications [66–68].

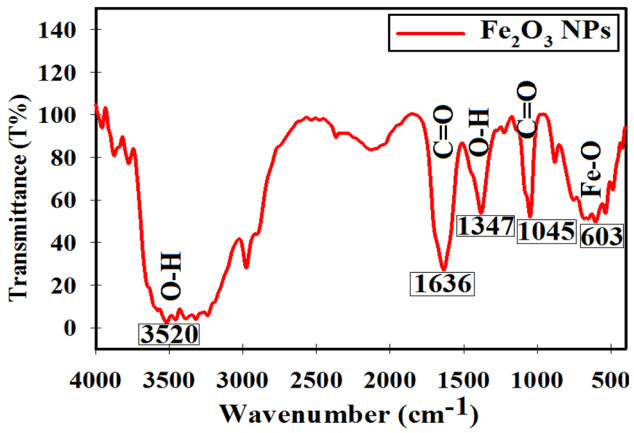

Fig. 14 Determination of OH surface function group by FTIR analysis of Fe_2O_3 NPs

3.4 Kinetic Parameters of HMX Nanocomposite Using Kissinger's Model

The thermal decomposition kinetics of HMX and Fe_2O_3/Al/HMX nanocomposite was investigated using TGA. Non-isothermal heating technique with four heating rates 2, 3, 4, 5 and 10 °C min^{-1} was employed (Fig. 15).

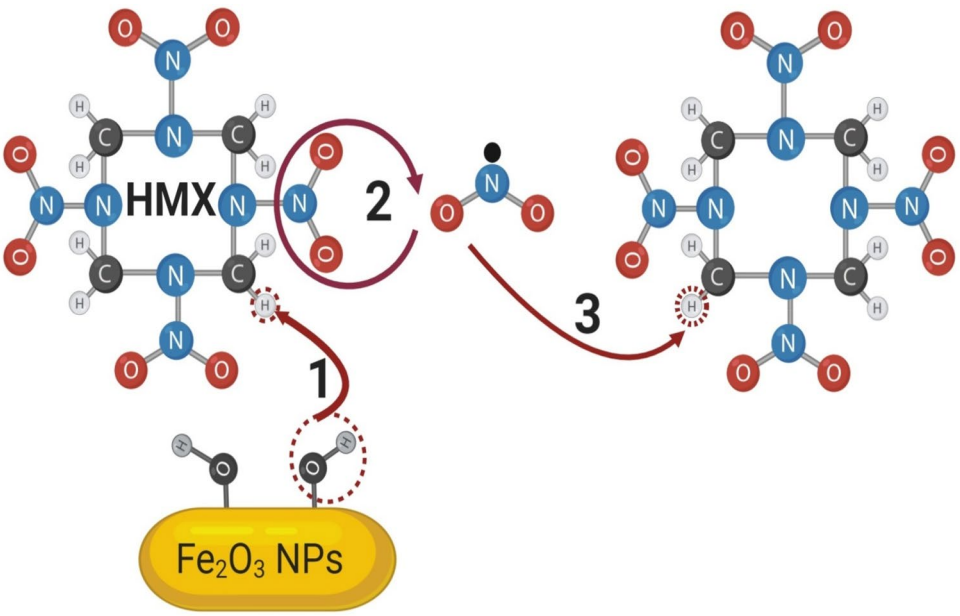

Fig. 13 Impact of thermite nanoparticles on HMX decomposition mechanism [9]

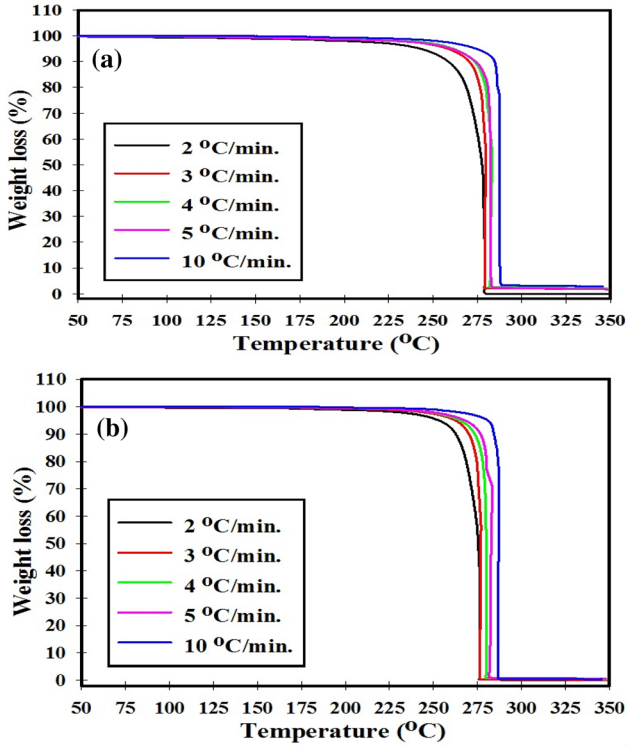

Fig. 15 TGA thermograms of different heating rates for HMX (**a**), and Fe_2O_3/Al/HMX nanocomposite (**b**)

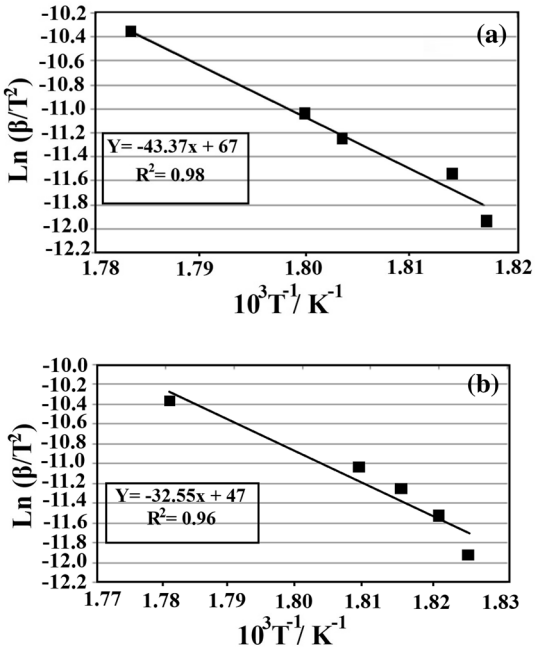

Fig. 16 Kissinger method to determine the activation energy of pure HMX (**a**), and Fe_2O_3/Al/HMX nanocomposites (**b**)

The impact of thermite nanoparticles on HMX activation energy was determined using the Kissinger method. The activation energy was obtained from the slop of the straight line from plotting ln (β/T^2) versus 1/T, where T is the decomposition peak temperature which was derived from the DTG thermogram (Fig. 16).

Whereas activation energy of pure HMX was 360.6 kJ mol^{-1}; HMX nanocomposite demonstrated activation energy of 270.6 kJ mol^{-1}. Nano-thermite particles offered decrease in the HMX activation energy by 25%. It can be concluded that thermite particles not only act as high energy density material but also it could act as a sensitizer with decrease in required activation energy. These findings shaded the light on thermite nanoparticles with excellent catalytic proficiency in order to increase HMX decomposition rate.

3.5 Kinetic Parameters Using Kissinger–Akahira–Sunose (KAS) Method

The activation energy at the different fractional conversion was determined by using modified Kissinger–Akahira–Sunose (KAS) method. The kinetics parameters of HMX and HMX nanocomposite were tabulated in Table 1.

The mean value of the activation energies of HMX and HMX nanocomposite were 345.4 kJ·mol^{-1} and 282 kJ·mol^{-1}, respectively. The result from that data is that finding that thermite nanoparticles have a dual effect as novel catalyst with decrease in activation energy and as high energy density material that would boost the heat output.

By making a broad comparison with the literature regarding the thermal decomposition of HMX using different nanomaterial-based composite, Reena Dubey et al. [10], synthesized, characterized and studied the catalytic behavior of Cu NPs on the thermal decomposition of HMX, and the result indicated that, Cu NPs lowers the energy of activation for thermal decomposition of HMX. Activation energy for ignition has also been found to be lowered in case of HMX. Other related study [69], stated that the fabrication of surface modified HMX@ polyaniline (PANI) core–shell composites enhanced the thermal properties and desensitization via in situ polymerization. Also, Zhao et al. [70], conducting the kinetic model of thermal decomposition of CL-20/HMX co-crystal for thermal safety prediction. On the other hand, Bekhti et al. [71], enhanced the thermal stability, optical and electrochemical properties of PANI-matrix containing Al_2O_3 hybrid materials which synthesized through in situ polymerization.

Table 1 Kinetic parameters of HMX and Fe_2O_3/Al/HMX nanocomposite using the (KAS) method

α reacted	HMX			Fe_2O_3/Al/HMX nanocomposite		
	Ea (kJ mol^{-1})	Log A (s^{-1})	r	Ea (kJ mol^{-1})	Log A (s^{-1})	r
0.05	124	13.7	0.972	174.3	18.6	0.981
0.1	142	15.3	0.983	171.8	18.1	0.975
0.15	170	17.8	0.986	182.1	19.0	0.982
0.2	201	20.8	0.989	210.1	21.7	0.99
0.25	245	25.1	0.990	239.4	24.6	0.984
0.3	289	29.3	0.982	265.4	27.0	0.974
0.35	330	33.2	0.983	273.6	27.8	0.986
0.4	351	35.2	0.994	281.8	28.6	0.990
0.45	369	36.9	0.986	295.3	29.9	0.976
0.5	387	38.6	0.996	311.2	31.4	0.978
0.55	396	39.5	0.986	341.9	34.3	0.983
0.6	378	37.7	0.994	283.6	28.7	0.976
0.65	420	41.7	0.988	296.8	29.9	0.986
0.7	424	42.0	0.998	317.3	31.9	0.993
0.75	423	41.9	0.999	326.9	32.8	0.995
0.8	435	43.0	0.998	330.0	33.1	0.986
0.85	449	44.3	0.999	329.6	33.0	0.984
0.9	455	44.8	0.999	337.1	33.7	0.984
Mean	345.4	33.4	–	282	28	–

4 Conclusion

This study proposed an alternative eco-friendly and facile approach for thermite nanoparticles production via hydrothermal processing. Colloidal Fe_2O_3/Al thermite nanomixture was effectively-integrated into HMX crystals via co-precipitation technique. Full validation was performed to analyze the shape, crystallinity, distribution, and the size of the produced thermite NPs, and HMX-thermite nano-mixtuer, which were shown to be bright spherical particles within nano-scale. A suggested reaction mechanism describing that, Fe_2O_3 NPs can offer high ability to release active ȮH radicals, and evolved radicals would be capable to abstract hydrogen atom from HMX, then the energy of N-NO_2 bond would be decreased; nitro group could be released more easily form HMX molecule, and finally the evolved NO_2 group could attack another HMX molecule and abstract an H-atom. Integration of thermite nanoparticles into HMX demonstrated dramatic change in its thermal behavior. The catalytic activity of thermite NPs was further evaluated with TGA and confirmed DSC outcomes, where a temperature at total weight loss was decreased by 13 °C. The thermal decomposition kinetics of HMX and Fe_2O_3/Al/HMX nanocomposite was investigated using TGA non-isothermal technique with four heating rate 2, 3, 4, 5 and 10 °C min^{-1}. The impact of thermite nanoparticles on HMX activation energy was determined using the Kissinger method. Nano-thermite particles offered decrease in HMX activation energy by 25%. Whereas activation energy of pure HMX was 360.6 kJ mol^{-1}; HMX nanocomposite demonstrated lower activation energy of 270.6 kJ mol^{-1}. The scientific soundness of this research concerns that the mean value of the activation energies of HMX and HMX nanocomposite were 345.4 kJ·mol^{-1} and 282 kJ·mol^{-1}, respectively. The results confirming that thermite nanoparticles have a dual effect as novel catalyst with decrease in activation and high energy density material that would boost the heat output.

Supplementary Information The online version contains supplementary material available at https://doi.org/10.1007/s10904-021-01916-3.

Acknowledgements The authors would like to thank Nanotechnology Research Center, School of Chemical Engineering, Military Technical College, Egyptian Armed Forces, and Zeiss microscope team in Cairo for their invaluable advice during this study. Figures 2 and 13 had been created by Biorender.com.

Compliance with Ethical Standards

Conflict of interest The authors declare that they have no conflict of interest.

References

1. S. Elbasuney, M. Yehia, Ammonium perchlorate encapsulated with TiO_2 nanocomposite for catalyzed combustion reactions. J. Inorg. Organomet. Polym Mater. **29**(4), 1349–1357 (2019)
2. S. Elbasuney, Novel colloidal nanothermite particles (MnO_2/Al) for advanced highly energetic systems. J. Inorg. Organomet. Polym Mater. **28**(5), 1793–1800 (2018)
3. S. Elbasuney et al., Novel high energy density material based on metastable intermolecular nanocomposite. J. Inorg. Organomet. Polym Mater. **30**(10), 3980–3988 (2020)
4. S. Elbasuney, G.S. El-Sayyad, The potentials of TiO_2 nanocatalyst on HMX thermolysis. J. Mater. Sci. **31**(17), 14930–14940 (2020)
5. A.M.A. Elghafour et al., Highly energetic nitramines: a novel platonizing agent for double-base propellants with superior combustion characteristics. Fuel **227**, 478–484 (2018)
6. S. Elbasuney et al., Chemical stability, thermal behavior, and shelf life assessment of extruded modified double-base propellants. Defence Technol. **14**(1), 70–76 (2018)
7. S. Elbasuney, M. Yehia, Ferric oxide colloid: a novel nano-catalyst for solid propellants. J. Inorg. Organomet. Polym. Mater. **30**(3), 706–713 (2020)
8. S. Elbasuney et al., Infrared signature of novel super-thermite (Fe_2O_3/Mg) fluorocarbon nanocomposite for effective countermeasures of infrared seekers. J. Inorg. Organomet. Polym Mater. **28**(5), 1718–1727 (2018)
9. V.E. Zarko, A.A. Gromov (eds.), *Energetic Nanomaterials Synthesis, Characterization, and Application* (Elsevier, Amsterdam, 2016)
10. R. Dubey et al., Synthesis, characterization and catalytic behavior of Cu nanoparticles on the thermal decomposition of AP, HMX, NTO and composite solid propellants, Part 83. Thermochim. Acta **549**, 102–109 (2012)
11. J. Wei et al., 0D Cu(II) and 1D mixed-valence Cu(I)/Cu(II) coordination compounds based on mixed ligands: Syntheses, structures and catalytic thermal decomposition for HMX. Inorg. Chem. Commun. **30**, 13–16 (2013)
12. S. Elbasuney, M. Gobara, M. Yehia, Ferrite nanoparticles: synthesis, characterization, and catalytic activity evaluation for solid rocket propulsion systems. J. Inorg. Organomet. Polym. Mater. **29**(3), 721–729 (2019)
13. S. Elbasuney, Steric stabilization of colloidal aluminium particles for advanced metalized-liquid rocket propulsion systems. Combust. Explos. Shock Waves **55**(3), 353–360 (2019)
14. S. Elbasuney, A. Fahd, Combustion wave of metalized extruded double-base propellants. Fuel **237**, 1274–1280 (2019)
15. K.R. Reddy et al., Synthesis of electrically conductive and superparamagnetic monodispersed iron oxide-conjugated polymer composite nanoparticles by in situ chemical oxidative polymerization. J. Colloid Interface Sci. **335**(1), 34–39 (2009)
16. K.R. Reddy et al., Self-assembly and graft polymerization route to monodispersed Fe_3O_4@ SiO_2—polyaniline core–shell composite nanoparticles: physical properties. J. Nanosci. Nanotechnol. **8**(11), 5632–5639 (2008)
17. K.R. Reddy, K.P. Lee, A.I. Gopalan, Novel electrically conductive and ferromagnetic composites of poly (aniline-co-aminonaphthalenesulfonic acid) with iron oxide nanoparticles: synthesis and characterization. J. Appl. Polym. Sci. **106**(2), 1181–1191 (2007)
18. K.R. Reddy et al., A new one-step synthesis method for coating multi-walled carbon nanotubes with cuprous oxide nanoparticles. Scripta Mater. **58**(11), 1010–1013 (2008)
19. C. Venkata Reddy et al., Synthesis and photoelectrochemical water oxidation of (Y, Cu) codoped α-Fe_2O_3 nanostructure photoanode. J. Alloy. Compd. **814**, 152349 (2020)
20. K. Kannan et al., Nanostructured metal oxides and its hybrids for photocatalytic and biomedical applications. Adv. Colloid Interface. Sci. **281**, 102178 (2020)
21. K.R. Reddy, K.-P. Lee, A.I. Gopalan, Self-assembly directed synthesis of poly (ortho-toluidine)-metal (gold and palladium) composite nanospheres. J. Nanosci. Nanotechnol. **7**(9), 3117–3125 (2007)
22. K. Raghava Reddy et al., Chapter 10 - Functionalized magnetic nanoparticles/biopolymer hybrids: synthesis methods, properties and biomedical applications, in *Methods in microbiology*. ed. by V. Gurtler, A.S. Ball, S. Soni (Academic Press, New York, 2019), pp. 227–254
23. M. Abd Elkodous et al., Fabrication of ultra-pure anisotropic zinc oxide nanoparticles via simple and cost-effective route: implications for UTI and EAC medications. Biol. Trace Elem. Res. **196**(1), 297–317 (2019)
24. C.V. Reddy et al., Z-scheme binary 1D $ZnWO_4$ nanorods decorated 2D $NiFe_2O_4$ nanoplates as photocatalysts for high efficiency photocatalytic degradation of toxic organic pollutants from wastewater. J. Environ. Manag. **268**, 110677 (2020)
25. M. Abd Elkodous, et al., Nanocomposite matrix conjugated with carbon nanomaterials for photocatalytic wastewater treatment. J. Hazard. Mater. 124657 (2020)
26. M.I.A. Abdel Maksoud et al., Nanostructured Mg substituted Mn-Zn ferrites: a magnetic recyclable catalyst for outstanding photocatalytic and antimicrobial potentials. J. Hazard. Mater. **399**, 123000 (2020)
27. T. Tavangar et al., Textile waste, dyes/inorganic salts separation of cerium oxide-loaded loose nanofiltration polyethersulfone membranes. Chem. Eng. J. **385**, 123787 (2020)
28. E. Haque et al., Nanoarchitectured Graphene-Organic Frameworks (GOFs): synthetic strategies, properties, and applications. Chemistry **13**(23), 3561–3574 (2018)
29. C.V. Reddy et al., Metal-organic frameworks (MOFs)-based efficient heterogeneous photocatalysts: synthesis, properties and its applications in photocatalytic hydrogen generation, CO_2 reduction and photodegradation of organic dyes. Int. J. Hydrogen Energy **45**(13), 7656–7679 (2020)
30. C.V. Reddy et al., Mn-doped ZrO_2 nanoparticles prepared by a template-free method for electrochemical energy storage and abatement of dye degradation. Ceram. Int. **45**(12), 15298–15306 (2019)
31. C.V. Reddy et al., Copper-doped ZrO_2 nanoparticles as high-performance catalysts for efficient removal of toxic organic pollutants and stable solar water oxidation. J. Environ. Manag. **260**, 110088 (2020)
32. C.V. Reddy et al., Efficient removal of toxic organic dyes and photoelectrochemical properties of iron-doped zirconia nanoparticles. Chemosphere **239**, 124766 (2020)
33. C.V. Reddy et al., Ni-dopant concentration effect of ZrO_2 photocatalyst on photoelectrochemical water splitting and efficient removal of toxic organic pollutants. Sep. Purif. Technol. **252**, 117352 (2020)
34. S.P. Dharupaneedi et al., Membrane-based separation of potential emerging pollutants. Sep. Purif. Technol. **210**, 850–866 (2019)
35. P.S. Basavarajappa et al., Enhanced photocatalytic activity and biosensing of gadolinium substituted $BiFeO_3$ nanoparticles. ChemistrySelect **3**(31), 9025–9033 (2018)
36. C.V. Reddy et al., Highly enhanced photoelectrocatalytic water oxidation using $BiVO_4$ nanostructures Novel $BiVO_4$ nanostructures for environmental remediation, enhanced photoelectrocatalytic water oxidation and electrochemical energy storage performance. Sol. Energy **207**, 41–449 (2020)
37. K. Karthik et al., Barium titanate nanostructures for photocatalytic hydrogen generation and photodegradation of chemical pollutants. J. Mater. Sci. **30**(23), 20646–20653 (2019)

38. R. Koutavarapu et al., ZnO nanosheets-decorated Bi_2WO_6 nanolayers as efficient photocatalysts for the removal of toxic environmental pollutants and photoelectrochemical solar water oxidation. J. Environ. Manag. **265**, 110504 (2020)
39. M. Srinivas et al., Novel Co and Ni metal nanostructures as efficient photocatalysts for photodegradation of organic dyes. Mater. Res. Express **6**(12), 125502 (2019)
40. S. Elbasuney et al., Facile synthesis of RGO-Fe_2O_3 nanocomposite: a novel catalyzing agent for composite propellants. J. Mater. Sci. **31**(23), 20805–20815 (2020)
41. S. Elbasuney et al., Stabilized super-thermite colloids: a new generation of advanced highly energetic materials. Appl. Surf. Sci. **419**, 328–336 (2017)
42. S. Elbasuney et al., Super-thermite (Al/Fe_2O_3) Fluorocarbon nanocomposite with stimulated infrared thermal signature via extended primary combustion zones for effective countermeasures of infrared seekers. J. Inorg. Organomet. Polym Mater. **28**(6), 2231–2240 (2018)
43. Q.-L. Yan et al., Catalytic effects of nano additives on decomposition and combustion of RDX-, HMX-, and AP-based energetic compositions. Prog. Energy Combust. Sci. **57**, 75–136 (2016)
44. S. Vyazovkin et al., ICTAC kinetics committee recommendations for performing kinetic computations on thermal analysis data. Thermochim. Acta **520**(1–2), 1–19 (2011)
45. D. Trache et al., Physicochemical properties of microcrystalline nitrocellulose from Alfa grass fibres and its thermal stability. J. Therm. Anal. Calorim. **124**(3), 1485–1496 (2016)
46. T. Akahira, Trans. Joint convention of four electrical institutes. Res. Rep. Chiba Inst. Technol. **16**, 22–31 (1971)
47. V.C. Karade et al., A green approach for the synthesis of α-Fe2O3 nanoparticles from Gardenia resinifera plant and it's In vitro hyperthermia application. Heliyon **5**(7), e02044 (2019)
48. D.E. Fouad et al., Improved size, morphology and crystallinity of hematite (α-Fe_2O_3) nanoparticles synthesized via the precipitation route using ferric sulfate precursor. Results Phys. **12**, 1253–1261 (2019)
49. M. Sharma, α-Fe_2O_3 preparation by sol-gel method, University of Delhi, Lab Manual (2017). https://www.bragitoff.com/wp-content/uploads/2017/09/fe2o3-xrd-compressed-ver-2.pdf
50. T. Liang et al., Design of functionalized α-Fe_2O_3 (III) films with long-term anti-wetting properties. Ceram. Int. **46**(5), 6129–6135 (2020)
51. M. Tadic et al., Magnetic properties of hematite (α– Fe_2O_3) nanoparticles synthesized by sol-gel synthesis method: the influence of particle size and particle size distribution. J. Electr. Eng. **70**(7), 71–76 (2019)
52. Q.Z. Zeng et al., Hydrothermal synthesis of monodisperse α-Fe_2O_3 hollow microspheroids and their high gas-sensing properties. J. Alloy. Compd. **705**, 427–437 (2017)
53. P. Belavi et al., Structural, electrical and magnetic properties of cadmium substituted nickel–copper ferrites. Mater. Chem. Phys. **132**(1), 138–144 (2012)
54. M.A. Maksoud et al., Synthesis and characterization of metals-substituted cobalt ferrite [M_x $Co_{(1-x)}$ Fe_2O_4;(M= Zn, Cu and Mn; x= 0 and 0.5)] nanoparticles as antimicrobial agents and sensors for Anagrelide determination in biological samples. Mater. Sci. Eng. C **92**, 644–656 (2018)
55. A. Ashour et al., Antimicrobial activity of metal-substituted cobalt ferrite nanoparticles synthesized by sol–gel technique. Particuology **40**, 141–151 (2018)
56. M.A. Maksoud et al., Tunable structures of copper substituted cobalt nanoferrites with prospective electrical and magnetic applications. J. Mater. Sci. **30**(5), 4908–4919 (2019)
57. K. Pal, M.A. Elkodous, M.M. Mohan, CdS nanowires encapsulated liquid crystal in-plane switching of LCD device. J. Mater. Sci. **29**(12), 10301–10310 (2018)
58. C. Mandilas et al., Synthesis of aluminium nanoparticles by arc plasma spray under atmospheric pressure. Mater. Sci. Eng. B **178**(1), 22–30 (2013)
59. M. Paskevicius et al., Mechanochemical synthesis of aluminium nanoparticles and their deuterium sorption properties to 2 kbar. J. Alloy. Compd. **481**(1–2), 595–599 (2009)
60. B. Alinejad, K. Mahmoodi, A novel method for generating hydrogen by hydrolysis of highly activated aluminum nanoparticles in pure water. Int. J. Hydrogen Energy **34**(19), 7934–7938 (2009)
61. A. Baraka et al., Synthesis of silver nanoparticles using natural pigments extracted from Alfalfa leaves and its use for antimicrobial activity. Chem. Pap. **71**(11), 2271–2281 (2017)
62. F.M. Mosallam et al., Biomolecules-mediated synthesis of selenium nanoparticles using *Aspergillus oryzae* fermented Lupin extract and gamma radiation for hindering the growth of some multidrug-resistant bacteria and pathogenic fungi. Microb. Pathog. **122**, 108–116 (2018)
63. J.J.-I. Yoh et al., Test-based thermal explosion model for HMX. Proc. Combust. Inst. **31**(2), 2353–2359 (2007)
64. C.M. Tarver, T.D. Tran, Thermal decomposition models for HMX-based plastic bonded explosives. Combust. Flame **137**(1), 50–62 (2004)
65. A.I. El-Batal et al., Nystatin-mediated bismuth oxide nano-drug synthesis using gamma rays for increasing the antimicrobial and antibiofilm activities against some pathogenic bacteria and *Candida* species. RSC Adv. **10**(16), 9274–9289 (2020)
66. H. Pouran et al., Assessment of ATR-FTIR spectroscopy with multivariate analysis to investigate the binding mechanisms of Ag and TiO_2 nanoparticles to Chelex®-100 or MetsorbTM for the DGT technique. Anal. Methods **12**(7), 959–969 (2020)
67. T. Munir et al., Impact of silver dopant on structural and optical properties of TiO_2 nanoparticles. Digest J. Nanomater. Biostruct. (DJNB) **14**(2), 279–284 (2019)
68. G.S. El-Sayyad et al., Merits of photocatalytic and antimicrobial applications of gamma-irradiated Co_x Ni_{1-x} Fe_2O_4/SiO_2/TiO_2; x= 09 nanocomposite for pyridine removal and pathogenic bacteria/fungi disinfection: implication for wastewater treatment. RSC Adv. **10**(9), 5241–5259 (2020)
69. S. Zhang et al., Fabrication and characterization of surface modified HMX@ PANI core-shell composites with enhanced thermal properties and desensitization via in situ polymerization. Appl. Surf. Sci. **515**, 146042 (2020)
70. L. Zhao et al., Kinetic model of thermal decomposition of CL-20/HMX co-crystal for thermal safety prediction. Thermochim. Acta **674**, 44–51 (2019)
71. M.A. Bekhti et al., Enhanced tailored of thermal stability, optical and electrochemical properties of PANI matrix containing Al_2O_3 hybrid materials synthesized through in situ polymerization. Polym. Compos. **42**(1), 6–14 (2021)